**Article**

# Efficient near-infrared harvesting in perovskite–organic tandem solar cells

https://doi.org/10.1038/s41586-025-09181-x

Received: 20 August 2024

Accepted: 21 May 2025

**Zhenrong Jia[1,2,9], Xiao Guo[1,2,9], Xinxing Yin[3,9], Ming Sun[4], Jiawei Qiao[4], Xinyu Jiang[5], Xi Wang[1,2], Yuduan Wang[1,2], Zijing Dong[1,2], Zhuojie Shi[1,2], Chun-Hsiao Kuan[6,7], Jingcong Hu[1,2], Qilin Zhou[1,2], Xiangkun Jia[1,2], Jinxi Chen[1,2], Zhouyin Wei[2], Shunchang Liu[1,2], Haoming Liang[1,2], Nengxu Li[1,2], Ling Kai Lee[2], Renjun Guo[2], Stephan V. Roth[5], Peter Müller-Buschbaum[8], Xiaotao Hao[4], Xiaoyan Du[4] & Yi Hou[1,2] ✉**

The broad bandgap tunability of both perovskites and organic semiconductors enables the development of perovskite–organic tandem solar cells with promising theoretical efficiency. However, the certified efficiencies of reported perovskite–organic tandem solar cells remain lower than those of single-junction perovskite solar cells, primarily because of insufficient near-infrared photocurrent in narrow-bandgap organic subcells[1–3]. Here we design and synthesize an asymmetric non-fullerene acceptor (NFA), P2EH-1V, featuring a unilateral conjugated π-bridge to reduce the optical bandgap to 1.27 eV while maintaining ideal exciton dissociation and nanomorphology. Transient absorption spectroscopy confirms efficient hole transfer from P2EH-1V to the donor PM6. Devices based on P2EH-1V exhibit reduced non-radiative voltage losses of 0.20 eV without compromising charge-generation efficiency. We achieve a 17.9% efficiency for the organic bottom cell, with a high short-circuit current density ($J_{sc}$) of 28.60 mA $cm^{-2}$. Furthermore, we minimize interface recombination losses, enabling the perovskite top cell to achieve an impressive open-circuit voltage ($V_{oc}$) of 1.37 V and a fill factor (FF) of 85.5%. These advancements result in perovskite–organic tandem solar cells achieving a record efficiency of 26.7% (certified at 26.4%) over an aperture area greater than 1 $cm^2$.

NFAs used in organic photovoltaics exhibit robust near-infrared absorption and notable bandgap tunability, making them ideal candidates for bottom cells in perovskite–organic tandem solar cells when paired with wide-bandgap (WBG) perovskite top cells[4,5]. This all-thin-film tandem configuration not only surpasses the Shockley–Queisser limit of both single-junction perovskite and organic photovoltaic cells but also offers enhanced operational stability owing to the ultraviolet-filtering properties of the perovskite layer[6–9]. Compared with perovskite–silicon, perovskite–copper indium gallium selenide (CIGS) and perovskite–perovskite tandems, the absorber layers of the two subcells in perovskite–organic tandems can be fully processed using high-throughput roll-to-roll techniques under consistent ambient conditions on flexible polymer substrates. Their light weight and potentially flexible design make them particularly well suited for applications such as building-integrated photovoltaics, vehicle-integrated photovoltaics, drones and consumer electronics[10].

Despite these advances, the highest-performing perovskite–organic tandem solar cells so far still fall short of achieving higher certified power conversion efficiencies (PCEs) compared with published single-junction perovskite cells (24.7%) and other reported perovskite thin-film tandems, such as perovskite–perovskite (28.2%) and perovskite–CIGS (24.2%) tandems, within the same active area (for example, 1 $cm^2$)[11–14]. A substantial challenge in advancing perovskite–organic tandems is the limited availability of efficient narrow-bandgap NFAs suitable for the organic bottom cell, which contributes to the relatively low photocurrent densities observed in these tandem devices[15,16]. For instance, the present dominant acceptor, Y6 (BTP-4F), used in the bottom cell of perovskite–organic tandems, has an optical bandgap of approximately 1.33 eV (ref. 17). Although this bandgap is ideal for single-junction solar cells, it is suboptimal for tandem configurations, in which the ideal bandgap for the bottom cell in dual-junction tandems is around 1.00 eV (ref. 18).

In previous studies, the bandgap of NFAs has been reduced by increasing the conjugation length or enhancing the intramolecular charge-transfer effect[19,20]. However, constructing narrow-bandgap NFAs typically requires greatly extending the conjugated backbone, which sharply increases the highest occupied molecular orbital (HOMO) energy levels[21,22]. This approach leads to an energy-level mismatch between the acceptors and polymer donors, negatively affecting exciton dissociation efficiency and overall external quantum efficiency (EQE)[23–26]. In this study, we design and synthesize a new asymmetric NFA, P2EH-1V, by strategically inserting an ethylene double bonds

---

[1] Department of Chemical and Biomolecular Engineering, National University of Singapore, Singapore, Singapore. [2] Solar Energy Research Institute of Singapore (SERIS), National University of Singapore, Singapore, Singapore. [3] China-Australia Institute for Advanced Materials and Manufacturing (IAMM), Jiaxing University, Jiaxing, China. [4] School of Physics, State Key Laboratory of Crystal Materials, Shandong University, Jinan, China. [5] Deutsches Elektronen-Synchrotron (DESY), Hamburg, Germany. [6] Department of Applied Chemistry, National Yang Ming Chiao Tung University, Hsinchu, Taiwan. [7] Institute of Molecular Science, National Yang Ming Chiao Tung University, Hsinchu, Taiwan. [8] Department of Physics, TUM School of Natural Sciences, Technical University of Munich, Garching, Germany. [9] These authors contributed equally: Zhenrong Jia, Xiao Guo, Xinxing Yin. ✉e-mail: yi.hou@nus.edu.sg

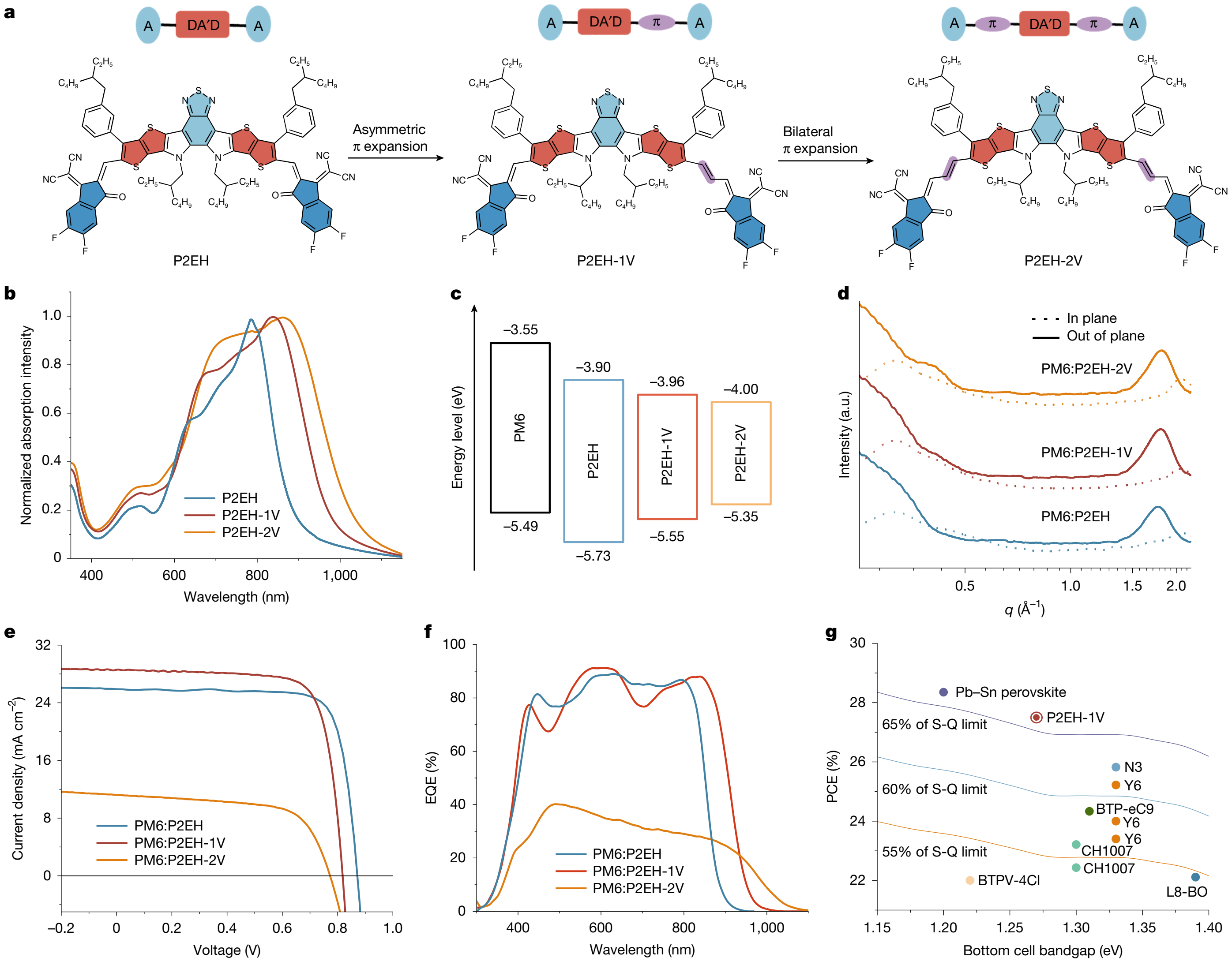

**Fig. 1 | NFA design and device performance. a**, The molecular structure of acceptors. **b**, Absorption spectra of the P2EH, P2EH-1V and P2EH-2V films. **c**, The energy-level diagram of PM6, P2EH, P2EH-1V and P2EH-2V neat films. **d**, Radial GIWAXS profiles integrated over in-plane ($30° < \chi < 90°$) and out-of-plane ($0° < \chi < 30°$) azimuthal angles for PM6:NFA blend films. **e**, Champion *J*–*V* curves of single-junction organic photovoltaic devices. **f**, EQE curves of single-junction organic photovoltaic devices. **g**, Comparisons between champion perovskite–organic tandem cells of this work and previous reports of perovskite–organic tandem cells with PCE ≥ 22% in terms of optical bandgap of acceptor versus PCE. a.u., arbitrary units; S-Q, Shockley–Queisser.

π-bridge between the central fused ring unit and the end groups of P2EH. This modification reduces the optical bandgap of the NFA to 1.27 eV while maintaining a sufficient energy-level difference with the high-efficiency donor PM6, ensuring efficient exciton separation.

## NFA design and photovoltaic performance

To realize an optimal NFA for application in perovskite–organic tandem solar cells, inserting the double bonds π-bridge into the NFAs is an effective strategy. Jia et al. reported an ultranarrow-bandgap NFA with double bonds π-bridge, achieving a bandgap below 1.2 eV and a record $J_{sc}$ exceeding 30 mA cm$^{-2}$ (ref. 27). However, this design method is limited by the constraints between the spectral redshift and the increase in the HOMO energy level, which is unfavourable for matching with high-performance donors, leading to the moderate $V_{oc}$ and FF (ref. 28). Here we design an asymmetric NFA P2EH-1V by unidirectionally extending the conjugation of P2EH (refs. 29,30). Introducing double bonds into the acceptor molecules can substantially increase the conjugation length, forming a larger π-conjugated system, thereby enhancing the delocalization of electrons[31,32]. In π-conjugated systems, electrons in the π orbitals are delocalized across the conjugated structure. By extending the conjugation by inserting double bonds, the electron density spreads over a larger area, leading to a reduction in the energy gap between the lowest unoccupied molecular orbital (LUMO) and the HOMO[33,34]. The molecular structures of P2EH, P2EH-1V and P2EH-2V are shown in Fig. 1a, Fig. 1b and Supplementary Fig. 1 show the normalized ultraviolet–visible absorption spectra of the three NFA films and solutions. Supplementary Fig. 2 shows the absorption coefficient of neat and blend film. As reported previously, P2EH shows an absorption onset of 890 nm and an optical bandgap of 1.39 eV. The absorption of P2EH-1V is redshifted about 80 nm compared with that of P2EH, corresponding to the optical bandgap of 1.27 eV. Owing to the further increased conjugation length, the absorption onset of P2EH-2V is redshifted to 1,033 nm with the bandgap of 1.20 eV. P2EH-1V and P2EH-2V deliver redshifted absorption spectra, which can broaden the light-harvesting window for higher $J_{sc}$ in perovskite–organic tandem cells.

Unlike the NFA P2EH-2V, in which double bonds are inserted on both sides, inserting double bonds unidirectionally allows for more precise control of the increase in the HOMO energy level. Cyclic voltammetry measurements are performed to estimate the electronic energy levels of the PM6 (PBDB-T-2F) and three NFAs. As expected, with the increase in the number of double bonds of the NFAs, the HOMO energy level gradually increases. The HOMO energy level/LUMO energy level values of PM6, P2EH, P2EH-1V and P2EH-2V are measured to be −5.49/−3.55, −5.73/−3.90, −5.55/−3.96 and −5.39/−4.00 eV, respectively (Fig. 1c, Supplementary Table 1 and Supplementary Fig. 3). Compared with P2EH, the HOMO energy level of P2EH-1V appropriately reduces the bandgap, while ensuring the exciton dissociation driving force. A negative donor–acceptor offset is found between PM6 and P2EH-2V, which could result in a poor hole-transfer process[35].

The crystalline behaviours of the different NFA-based films are characterized by the grazing-incidence wide-angle X-ray scattering (GIWAXS) profiles. A detailed explanation of radial GIWAXS profiles is provided in Supplementary Note 1. All acceptors exhibit a preferential face-on orientation with comparable coherence lengths, as shown in Supplementary Figs. 4 and 5. For PM6:NFA blends (Fig. 1d and Supplementary Fig. 6), the coherence lengths of the (010) diffraction peaks for the three blended films are comparable. These consistent comparable coherence length values indicate that introducing double bonds into P2EH does not greatly disrupt the packing of the original ordered acceptors. This underscores the potential of P2EH-1V to achieve a comparable FF to P2EH while simultaneously reducing the bandgap[36]. The subtracted parameters from 2D GIWAXS images are summarized in Supplementary Tables 2 and 3. The surface morphology for the different blends is evaluated by atomic force microscopy (AFM), as shown in Supplementary Fig. 7. The active layers based on the three acceptors exhibit similar surface roughness. Contact-angle measurements indicate that compatibility decreases as the number of double bonds in the acceptor increases (Supplementary Fig. 8 and Supplementary Table 4). Transmission electron microscopy analysis further reveals that increasing the number of double bonds results in more pronounced phase separation between the donor and the acceptor in the active layers. For the PM6:P2EH-1V blend films, marginally larger bright and dark patterns are observed compared with the PM6:P2EH blend films. By contrast, much more pronounced bright and dark patterns are evident in the PM6:P2EH-2V blend films. These findings suggest that PM6:P2EH-1V blend films remain within a favourable phase-separation regime, which promotes efficient exciton dissociation, whereas PM6:P2EH-2V blend films exhibit excessive phase separation (Supplementary Fig. 9).

To take advantage of superiorities brought by the broader absorption range of P2EH-1V, we fabricate single-junction organic solar cells based on the structure of indium tin oxide (ITO)/$MoO_x$/PM6:NFA/PDINN/Ag. Figure 1e shows the champion $J$–$V$ characteristics and Supplementary Table 5 summarizes their photovoltaic parameters. The device based on PM6:P2EH achieves a maximum PCE of 17.5% with a $V_{oc}$ of 0.88 V, $J_{sc}$ of 25.72 mA cm$^{-2}$ and a FF of 77.2%. Encouragingly, the PM6:P2EH-1V-based organic solar cell achieves a PCE of 17.9% with a $V_{oc}$ of 0.82 V, a higher $J_{sc}$ of 28.60 mA cm$^{-2}$ and a FF of 76.5%. The enhanced $J_{sc}$ resulted from the obviously redshifted absorption of P2EH-1V. Although the absorption spectrum of P2EH-2V is further broadened, the device shows a much lower PCE of 5.6% with a low $J_{sc}$ of 11.21 mA cm$^{-2}$ and a FF of 64.8%, which can be ascribed to HOMO level mismatch with PM6. The photovoltaic parameters statistics and corresponding EQE plots of the P2EH, P2EH-1V and P2EH-2V devices are shown in Supplementary Fig. 10 and Fig. 1f. The integrated current densities derived from the EQE plots are 25.12, 27.86 and 11.06 mA cm$^{-2}$, respectively, which match well with those afforded by $J$–$V$ tests (within 3% error). Compared with previous reports of NFAs used in perovskite–organic tandem cells, as summarized in Fig. 1g and Supplementary Table 6, P2EH-1V demonstrates superior optical bandgap and photovoltaic performance, making it a promising acceptor for constructing the bottom cell in perovskite–organic tandem cells.

To further assess the charge dynamics of different blends, we use femtosecond transient absorption spectroscopy measurement to evaluate the hole-transfer process from NFAs to the donor[37]. The negative signals at 500–670 nm can be assigned to the ground-state bleaching (GSB) of PM6, at which no GSB signals are observed from the neat acceptor films (Fig. 2a–c and Supplementary Figs. 11–13). Here GSB kinetics of PM6 are used on behalf of hole-transfer dynamics, which mainly adopts the interfacial charge-transfer state dissociation. Therefore, the hole-transfer process can be assessed by fits to the donor GSB (575 nm) traces with a double exponential function, as shown in Fig. 2d. For PM6:P2EH and PM6:P2EH-1V blends, prominent bleaching signals emerge in both blends. This observation indicates a rapid and efficient hole-transfer process from the acceptor to the donor, which is consistent with the high EQE response for both cases. By contrast, very weak GSB signals appear in the PM6:P2EH-2V blend. This finding implies that the hole transfer from P2EH-2V to PM6 is minimal. The potential barrier between the HOMO levels of P2EH-2V and PM6 leads to a much slower hole-transfer rate compared with PM6:P2EH-1V. This behaviour suggests that the hole transfer from the acceptor P2EH-2V to the donor PM6 is negligible.

The charge dissociation probability ($P_{diss}$) for all devices is calculated from the photoinduced current density against effective voltage plots (Fig. 2e). The PM6:P2EH-based and PM6:P2EH-1V-based devices exhibit the highest $P_{diss}$ of 96.4% and 96.1%, respectively, enabling a high charge-generation probability and consequently yielding the excellent EQE response. By contrast, a low $P_{diss}$ of 85.1% is observed in the PM6:P2EH-2V-based device, which indicates the poor exciton dissociation behaviour. The impedance spectroscopy results revealed that the P2EH-based and P2EH-1V-based devices exhibit a much higher recombination resistance compared with the P2EH-2V-based device (Supplementary Fig. 14). This result indicates that the P2EH-2V-based device exhibits more severe charge recombination compared with the P2EH-based and P2EH-1V-based devices.

To investigate the influence of varying the number of π-bridges on the energy loss of NFAs, a detailed energy-loss analysis is conducted (Fig. 2f–i), with the relevant data summarized in Fig. 2f and Supplementary Table 7. Compared with the P2EH-based device, the P2EH-1V-based device exhibited a 0.05 eV reduction in energy loss, primarily because of a decrease in non-radiative energy loss from 0.26 eV to 0.20 eV (Supplementary Fig. 15). Reducing the HOMO offset between the donor and acceptor effectively lowers non-radiative recombination[38,39]. However, in PM6:P2EH-2V, the negative HOMO offset, although further suppressing non-radiative recombination, greatly hinders exciton dissociation and photocurrent generation. This phenomenon results from a shift in the charge transfer–locally excited equilibrium towards the acceptor's locally excited states, leading to dominant recombination by means of the higher-emission locally excited states instead of the charge-transfer states[40], thereby reducing non-radiative energy loss. This result confirms that unidirectionally inserting π-bridges can effectively reduce the energy loss of the device while simultaneously broadening the photoresponse.

## WBG perovskite subcell

With all of the advantages discussed above, it is attractive to transfer the PM6:P2EH-1V bottom cell to perovskite–organic tandem cells. The expected most suitable bandgap for perovskite front cell should be around 1.8 eV. However, state-of-the-art WBG perovskite cells suffer from substantial voltage and FF losses. To address these issues, we develop a self-assembled monolayer (SAM) of Br-Ph-4PACz by modification of Me-4PACz with introducing bromo-phenyl substitution instead of methyl substitution on the carbazole. The Br atom with strong electron affinity can effectively reduce work function and HOMO level, which can improve the band alignment with WBG perovskites[41] (Supplementary Fig. 16). Furthermore, the steric hindrance of benzene ring can inhibit excessive aggregation of molecules, thereby enhancing the uniformity of the hole-transporting layer and perovskite growth[42].

We use ultraviolet photoelectron spectroscopy to assess the energetic alignment of 1.8-eV perovskites and SAMs[43] (Fig. 3b, Supplementary

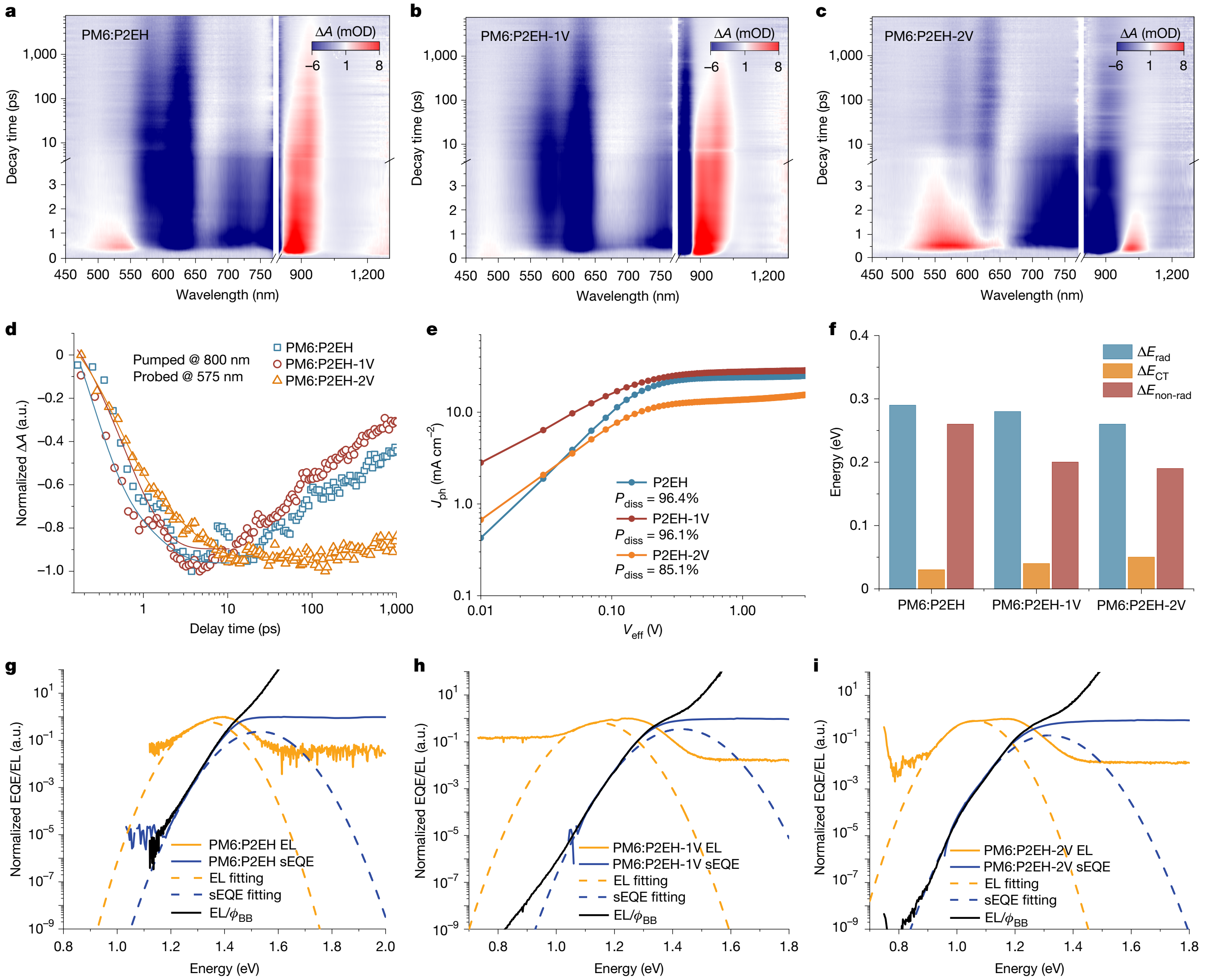

**Fig. 2 | Charge dynamics and energy-loss analysis. a**–**c**, Femtosecond transient absorption spectra of PM6:P2EH (**a**), PM6:P2EH-1V (**b**) and PM6:P2EH-2V (**c**) blend films. **d**, The trace kinetic of donor GSB signal probed at 575 nm. **e**, Characteristics of the photocurrent density versus effective voltage ($J_{ph}$–$V_{eff}$). **f**, Summary of $E_{loss}$ analysis of the corresponding organic solar cells. **g**–**i**, Gaussian fits of Fourier transform photocurrent spectroscopy EQE and electroluminescence (EL) curves by means of the Marcus equation for devices based on PM6:P2EH (**g**), PM6:P2EH-1V (**h**) and PM6:P2EH-2V (**i**) blends. a.u., arbitrary units.

Fig. 17 and Supplementary Table 8). Br-Ph-4PACz features a much deeper work function and a favourable energy alignment with the perovskite, compared with the Me-4PACz, which can lead to a mitigated energy loss at the interface for the solar cell devices. Kelvin probe force microscopy (KPFM) further corroborates the reduced work function of Br-Ph-4PACz on ITO substrate (Supplementary Fig. 18).

We conduct steady-state photoluminescence (PL) measurements and, as shown in Fig. 3c, the perovskite film on Br-Ph-4PACz exhibits a PL intensity that is five times higher than the perovskite film on Me-4PACz, suggesting reduced non-radiative recombination in the perovskite. Furthermore, we calculate the photoluminescence quantum yield (PLQY) for both conditions, revealing a marked increase from 0.41% for the Me-4PACz-based film to 1.82% for the Br-Ph-4PACz-based film. We also extract quasi-Fermi-level splitting and pseudo-$J$–$V$ of perovskite on different SAMs, which is directly related to the $V_{oc}$ of device (Fig. 3d,e and Supplementary Figs. 19–21). Perovskite on Br-Ph-4PACz shows an implied open-circuit voltage (i$V_{oc}$) of 1.38 V, which is higher than that in the perovskite/Me-4PACz stack (1.34 V), indicating a lower voltage loss at the interface between Br-Ph-4PACz and perovskites. Moreover, the Br-Ph-4PACz-based device shows a shorter photocurrent decay lifetime of 0.73 μs than the Me-4PACz-based device (0.87 μs), indicating improved charge-carrier extractions in the Br-Ph-4PACz-based device (Fig. 3f).

We measure contact angles to study the wetting properties of the different SAMs (Supplementary Fig. 22). The Br-Ph-4PACz-based substrate shows a greatly decreased contact angle of 10.4° compared with Me-4PACz (24.4°), indicating that the Br-Ph-4PACz enabled better wetting for uniform coverage of the perovskite film. We conduct confocal PL mapping to assess the uniformity of perovskite deposited on different SAMs. The results show that the perovskite film on Br-Ph-4PACz exhibits an improved PL emission intensity and homogeneity (Fig. 3g). This result indicates a notable enhancement in both the uniformity and the optoelectronic quality of perovskite grown on Br-Ph-4PACz.

To take advantage of superiorities brought by the reduced voltage loss and improved uniformity, we fabricate single-junction WBG perovskite solar cells. Figure 3i and Supplementary Fig. 23 show the $J$–$V$ curve of both 0.05-cm$^2$ Me-4PACz-based and Br-Ph-4PACz-based devices. Br-Ph-4PACz-based devices show a champion PCE of 20.4%, with a high $V_{oc}$ of 1.37 V and a FF of 85.5%. The statistical distributions

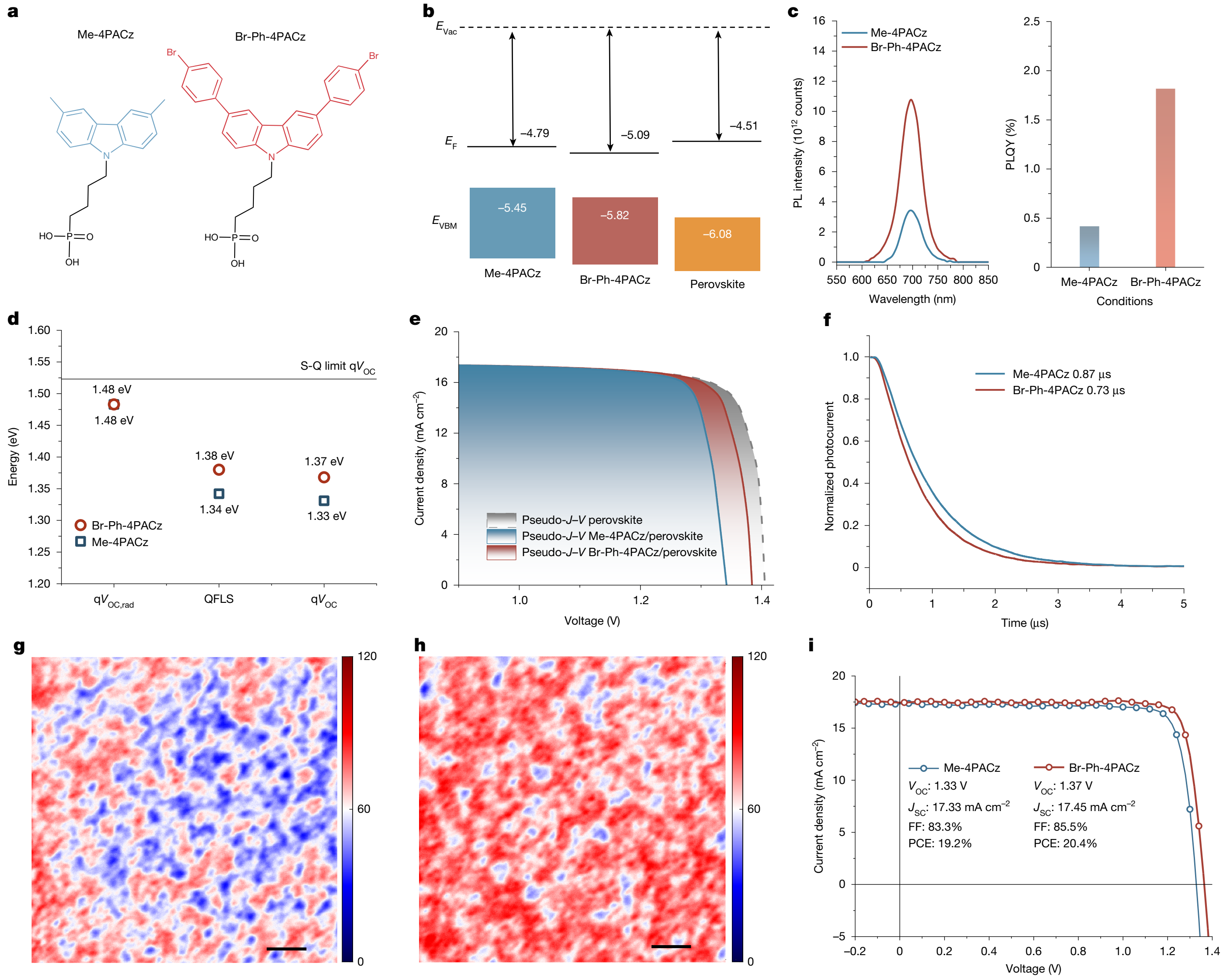

**Fig. 3 | Single-junction WBG perovskite solar cells. a**, Molecular structure of Me-4PACz and Br-Ph-4PACz. **b**, Energy-band alignment between perovskite with Me-4PACz and Br-Ph-4PACz. **c**, Steady-state PL spectra of perovskite (left) and calculated PLQY comparison (right) for perovskite film on Me-4PACz and Br-Ph-4PACz. **d**, $V_{oc}$ loss analysis for single-junction WBG perovskite solar cells. **e**, Pseudo-*J*–*V* curves obtained from intensity-dependent $V_{oc}$ and quasi-Fermi-level splitting (QFLS) measurements on the neat perovskite and the SAMs/perovskite. **f**, Transient photocurrent decays of Me-4PACz and Br-Ph-4PACz perovskite solar cells. The results are fitted with a single-exponential function. **g**, Confocal PL mapping image of perovskite film on Me-4PACz. Scale bar, 1 µm. **h**, Confocal PL mapping image of perovskite film on Br-Ph-4PACz. Scale bar, 1 µm. **i**, *J*–*V* scans of Me-4PACz and Br-Ph-4PACz based perovskite solar cells. S-Q, Shockley–Queisser.

of these devices agreed well with better PCE (Supplementary Fig. 24). By contrast, the Me-4PACz-based devices show moderate $V_{oc}$ and FF of 1.33 V and 83.3%, respectively, resulting in a PCE of 19.2%. The results of EQE measurements show high EQE response of both devices and are in line with $J_{sc}$ values obtained from *J*–*V* scans (Supplementary Fig. 25).

To further investigate the stability of WBG perovskites based on the different SAMs, we first tracked the evolution of PL spectra for both conditions by exposing perovskite films to continuous 1-sun 532-nm laser illumination (Supplementary Fig. 26). After 10 min of continuous illumination, both WBG perovskite thin films on the two SAMs exhibited phase segregation, as evidenced by the emergence of a new PL peak centred at approximately 760 nm. Compared with Me-PACz-based films, the phase segregation in Br-Ph-4PACz-based films is notably mitigated, as evidenced by the much lower intensity of the new PL peak at 760 nm in Br-Ph-4PACz-based films. This result indicates a more homogenous growth and higher quality of the perovskite layer on Br-Ph-4PACz, which could reduce the halide segregation of perovskite film. The AFM results show that Br-Ph-4PACz-based films exhibit a more uniform surface morphology, with a lower root-mean-square roughness of 18.9 nm, compared with the higher root-mean-square roughness of 22.2 nm observed in Me-4PACz-based films, indicating better film quality of the perovskite layer on Br-Ph-4PACz (Supplementary Fig. 27). Furthermore, we also tested the long-term stabilities of WBG perovskite devices at maximum power point (MPP) under illumination from a 100 mW cm$^{-2}$ white light-emitting diode (LED) at ambient atmosphere (Supplementary Fig. 28). The $T_{80}$ of the Me-4PACz-based device measured to be approximately 280 h. However, the $T_{80}$ of the device with Br-Ph-4PACz could be extended to 550 h, suggesting the positive effect of suppressed phase segregation on the MPP stabilities of WBG perovskite solar cell devices.

## Perovskite–organic tandem solar cells

Encouraged by the broadened absorption of the bottom cell and the good homogeneity of the front cell, we fabricate perovskite–organic

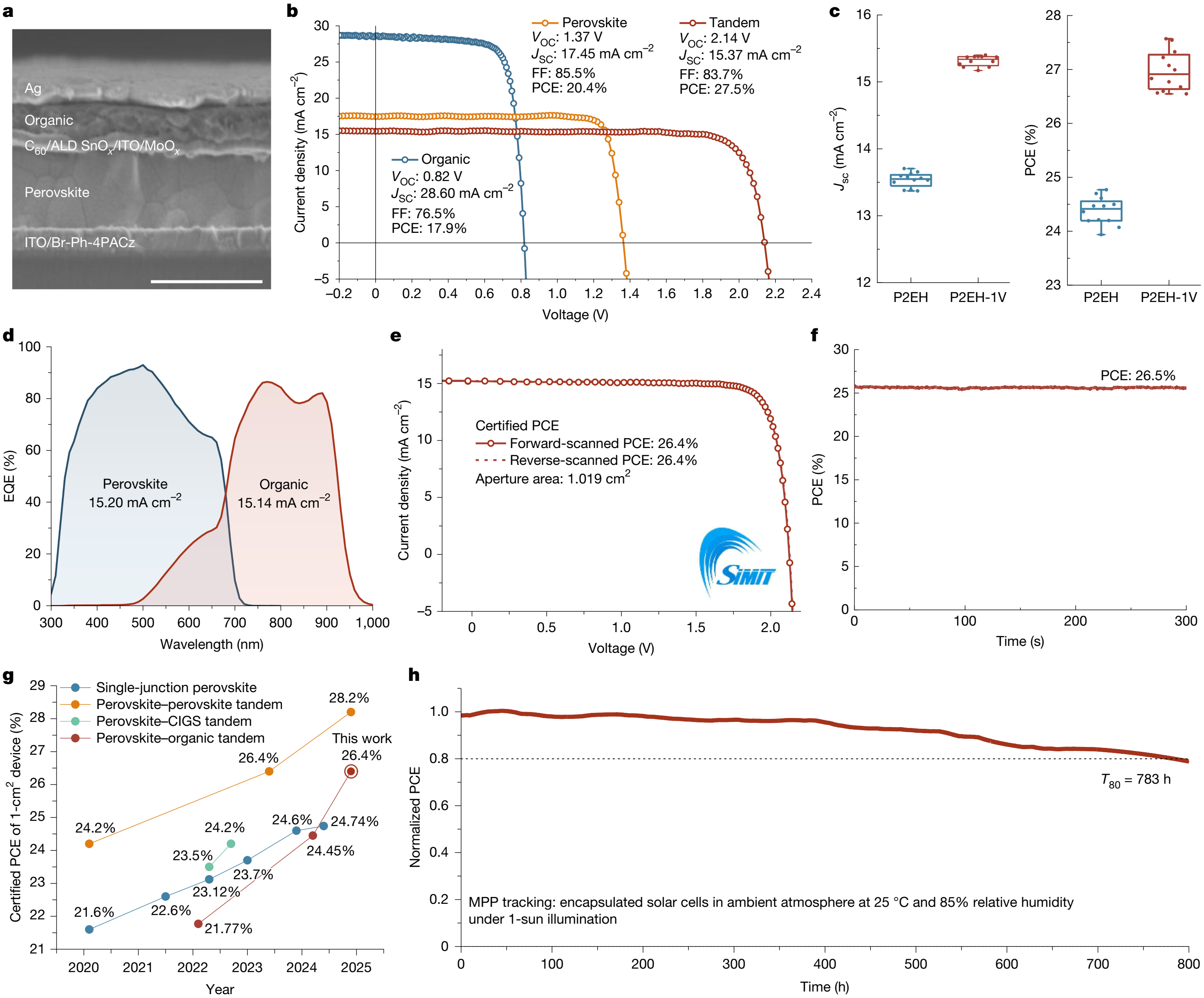

**Fig. 4 | Perovskite–organic tandem cells with P2EH-1V and Br-Ph-4PACz.** **a**, Cross-sectional scanning electron microscopy image of a perovskite–organic tandem cell. Scale bar, 500 nm. **b**, Combination of champion *J*–*V* curves and photovoltaic parameters of single-junction organic photovoltaic cells, perovskite solar cells and perovskite–organic tandem cells. **c**, Statistical distributions of $J_{sc}$ (left) and PCE (right) of perovskite–organic tandem cells with different NFAs (12 devices for each type). **d**, EQE curves and integrated $J_{sc}$ for perovskite and organic subcell in perovskite–organic tandem cells, respectively. **e**, *J*–*V* curve of the best 1-cm$^2$ perovskite–organic tandem cells certified by SIMIT. **f**, MPP tracking measurement of the champion 1-cm$^2$ device. **g**, Summary of the reported, independently certified PCEs of centimetre-scale single-junction perovskite solar cells, perovskite–perovskite tandem cells, perovskite–CIGS tandem cells and perovskite–organic tandem cells. **h**, Long-term MPP tracking results of perovskite–organic tandem cells.

tandems with the device architecture of glass/ITO/SAM/perovskite/$C_{60}$/$SnO_x$/ITO/$MoO_x$/organic/PDINN/Ag. The thicknesses of the perovskite and organic absorber layers for the front and bottom subcells were optimized to be approximately 290 and 110 nm (Fig. 4a), respectively, to obtain a well-balanced current density between the subcells. Figure 4b and Supplementary Fig. 29 presents the *J*–*V* curves of the best performing perovskite–organic tandems with different organic absorbers (PM6:P2EH and PM6:P2EH-1V). The statistical results also show that the substantial increase in $J_{sc}$ is the main factor for the improvement in efficiency (Fig. 4c and Supplementary Fig. 30). Notably, compared with the PM6:Y6-based device, the PM6:P2EH-1V-based device also boosts the efficiency from 25.8% to 27.5% with a $V_{oc}$ of 2.14 V, $J_{sc}$ of 15.37 mA cm$^{-2}$ and a FF of 83.7% (Supplementary Fig. 31). This value is the highest PCE reported for perovskite–organic tandem cells so far. The integrated $J_{sc}$ values from EQE measurements for the top and bottom cells are 15.20 mA cm$^{-2}$ and 15.14 mA cm$^{-2}$ (Fig. 4d), in good agreement with the $J_{sc}$ determined from *J*–*V* measurements. Notably, P2EH-1V exhibits substantially broadened near-infrared absorption and achieves a markedly higher integrated $J_{sc}$. Furthermore, we also demonstrate a PCE of 26.7%, $V_{oc}$ of 2.14 V, $J_{sc}$ of 15.15 mA cm$^{-2}$ and a FF of 82.4% for perovskite–organic tandem with an active area of 1.019 cm$^2$ (Supplementary Fig. 32), showing great potential for scaling up. We also sent the 1-cm$^2$ device to an accredited independent photovoltaics calibration laboratory (Shanghai Institute of Microsystem and Information Technology, SIMIT) for certification, and a certified PCE of 26.4% is obtained with no hysteresis (Fig. 4e and Supplementary Fig. 33), agreeing well with the value measured in the lab. Also, maximum point tracking efficiency is tested within 300 s continuous tracking and the 1-cm$^2$ perovskite–organic tandem device can still achieve a stabilized PCE of 26.5% (Fig. 4f). As shown in Fig. 4g and Supplementary Table 9, this certified PCE surpasses all certified PCEs for centimetre-scale single-junction perovskite solar cells, perovskite–CIGS tandem cells and perovskite–organic tandem cells.

We also evaluate the long-term stability of perovskite–organic tandem cells in ambient atmosphere (25 °C, 85% relative humidity), which is harsher than ISOS-L-1 protocols (Fig. 4h). The encapsulated perovskite–organic tandem cells retain 80% of their initial efficiency after 783 h of MPP tracking under continuous 1-sun LED illumination at a relative humidity of 85%. The $T_{80}$ of the single-junction organic photovoltaic cell is only 180 h (Supplementary Fig. 34), demonstrating the potential of tandem structures in improving organic photovoltaics stability. This improvement is primarily because of the ultraviolet-filtering effect of the front WBG perovskite layer, which reduces the degradation of organic materials caused by high-energy photons. To achieve longer stability, strategies such as suppressing the phase segregation in WBG perovskite, stabilizing the bulk heterojunction morphology and developing robust interfacial layers for organic subcells, will be pursued in the future.

## Online content

Any methods, additional references, Nature Portfolio reporting summaries, source data, extended data, supplementary information, acknowledgements, peer review information; details of author contributions and competing interests; and statements of data and code availability are available at https://doi.org/10.1038/s41586-025-09181-x.

1. Brinkmann, K. O. et al. Perovskite–organic tandem solar cells. *Nat. Rev. Mater.* **9**, 202–217 (2024).
2. Brinkmann, K. O. et al. Perovskite–organic tandem solar cells with indium oxide interconnect. *Nature* **604**, 280–286 (2022).
3. Chen, W. et al. Monolithic perovskite/organic tandem solar cells with 23.6% efficiency enabled by reduced voltage losses and optimized interconnecting layer. *Nat. Energy* **7**, 229–237 (2022).
4. Lin, Y. et al. An electron acceptor challenging fullerenes for efficient polymer solar cells. *Adv. Mater.* **27**, 1170–1174 (2015).
5. Meng, L. et al. Organic and solution-processed tandem solar cells with 17.3% efficiency. *Science* **361**, 1094–1098 (2018).
6. Chen, W. et al. A semitransparent inorganic perovskite film for overcoming ultraviolet light instability of organic solar cells and achieving 14.03% efficiency. *Adv. Mater.* **30**, 1800855 (2018).
7. Zhang, Z. et al. Suppression of phase segregation in wide-bandgap perovskites with thiocyanate ions for perovskite/organic tandems with 25.06% efficiency. *Nat. Energy* **9**, 592–601 (2024).
8. Chen, X. et al. Efficient and reproducible monolithic perovskite/organic tandem solar cells with low-loss interconnecting layers. *Joule* **4**, 1594–1606 (2020).
9. Wang, X. et al. Highly efficient perovskite/organic tandem solar cells enabled by mixed-cation surface modulation. *Adv. Mater.* **35**, 2305946 (2023).
10. Ho-Baillie, A. W. Y. et al. Recent progress and future prospects of perovskite tandem solar cells. *Appl. Phys. Rev.* **8**, 041307 (2021).
11. Jiang, X. et al. Isomeric diammonium passivation for perovskite–organic tandem solar cells. *Nature* **635**, 860–866 (2024).
12. Chen, H. et al. Improved charge extraction in inverted perovskite solar cells with dual-site-binding ligands. *Science* **384**, 189–193 (2024).
13. Wang, Y. et al. Homogenized contact in all-perovskite tandems using tailored 2D perovskite. *Nature* **635**, 867–873 (2024).
14. Jost, M. et al. Perovskite/CIGS tandem solar cells: from certified 24.2% toward 30% and beyond. *ACS Energy Lett.* **7**, 1298–1307 (2022).
15. He, Z. et al. Minimized optical/electrical energy loss for 25.1% monolithic perovskite/organic tandem solar cells. *Nat. Commun.* **16**, 1773 (2025).
16. Wu, S., Liu, M. & Jen, A. K. Y. Prospects and challenges for perovskite–organic tandem solar cells. *Joule* **7**, 484–502 (2023).
17. Yuan, J. et al. Single-junction organic solar cell with over 15% efficiency using fused-ring acceptor with electron-deficient core. *Joule* **3**, 1140–1151 (2019).
18. Leijtens, T. et al. Opportunities and challenges for tandem solar cells using metal halide perovskite semiconductors. *Nat. Energy* **3**, 828–838 (2018).
19. Wang, J. et al. The principles, design and applications of fused-ring electron acceptors. *Nat. Rev. Chem.* **6**, 614–634 (2022).
20. Cheng, P. & Yang, Y. Narrowing the band gap: the key to high-performance organic photovoltaics. *Acc. Chem. Res.* **53**, 1218–1228 (2020).
21. Liu, W. et al. Design of near-infrared nonfullerene acceptor with ultralow nonradiative voltage loss for high-performance semitransparent ternary organic solar cells. *Angew. Chem. Int. Ed.* **61**, e202116111 (2022).
22. Jia, Z. et al. High performance tandem organic solar cells via a strongly infrared-absorbing narrow bandgap acceptor. *Nat. Commun.* **12**, 178 (2021).
23. Chen, Z. et al. Ultrafast energy transfer from polymer donors facilitating spectral uniform photocurrent generation and low energy loss in high-efficiency nonfullerene organic solar cells. *Energy Environ. Sci.* **16**, 3373–3380 (2023).
24. Sun, C. et al. Achieving fast charge separation and low nonradiative recombination loss by rational fluorination for high-efficiency polymer solar cells. *Adv. Mater.* **31**, 1905480 (2019).
25. Liu, Y. et al. Recent progress in organic solar cells (Part I material science). *Sci. China Chem.* **65**, 224–268 (2022).
26. Yi, J. et al. Advantages, challenges and molecular design of different material types used in organic solar cells. *Nat. Rev. Mater.* **9**, 46–62 (2024).
27. Jia, Z. et al. Near-infrared absorbing acceptor with suppressed triplet exciton generation enabling high performance tandem organic solar cells. *Nat. Commun.* **14**, 1236 (2023).
28. Qin, S. et al. Constructing monolithic perovskite/organic tandem solar cell with efficiency of 22.0% via reduced open-circuit voltage loss and broadened absorption spectra. *Adv. Mater.* **34**, 2108829 (2022).
29. Zhang, J. et al. Alkyl-chain branching of non-fullerene acceptors flanking conjugated side groups toward highly efficient organic solar cells. *Adv. Energy Mater.* **11**, 2102596 (2021).
30. Kong, X. et al. 18.55% efficiency polymer solar cells based on a small molecule acceptor with alkylthienyl outer side chains and a low-cost polymer donor PTQ10. *CCS Chem.* **5**, 841–850 (2023).
31. Hai, J. et al. Achieving ultra-narrow bandgap non-halogenated non-fullerene acceptors via vinylene π-bridges for efficient organic solar cells. *Mater. Adv.* **2**, 2132–2140 (2021).
32. Li, X. et al. Synthesis and photovoltaic properties of a series of narrow bandgap organic semiconductor acceptors with their absorption edge reaching 900 nm. *Chem. Mater.* **29**, 10130–10138 (2017).
33. Liu, W. et al. Low-bandgap non-fullerene acceptors enabling high-performance organic solar cells. *ACS Energy Lett.* **6**, 598–608 (2021).
34. Shi, W. & Ma, H. Spectroscopic probes with changeable π-conjugated systems. *Chem. Commun.* **48**, 8732–8744 (2012).
35. Bertrandie, J. et al. The energy level conundrum of organic semiconductors in solar cells. *Adv. Mater.* **34**, 2202575 (2022).
36. Zhu, L. et al. Achieving 20.8% organic solar cells via additive-assisted layer-by-layer fabrication with bulk pin structure and improved optical management. *Joule* **8**, 3153–3168 (2024).
37. Li, S. et al. Highly efficient fullerene-free organic solar cells operate at near zero highest occupied molecular orbital offsets. *J. Am. Chem. Soc.* **141**, 3073–3082 (2019).
38. Xie, Y. et al. Assessing the energy offset at the electron donor/acceptor interface in organic solar cells through radiative efficiency measurements. *Energy Environ. Sci.* **12**, 3556–3566 (2019).
39. Xu, Y. et al. Tuning the hybridization of local exciton and charge-transfer states in highly efficient organic photovoltaic cells. *Angew. Chem. Int. Ed.* **59**, 9004–9010 (2020).
40. Classen, A. et al. The role of exciton lifetime for charge generation in organic solar cells at negligible energy-level offsets. *Nat. Energy* **5**, 711–719 (2020).
41. Yi, Z. et al. Achieving a high open-circuit voltage of 1.339 V in 1.77 eV wide-bandgap perovskite solar cells via self-assembled monolayers. *Energy Environ. Sci.* **17**, 202–209 (2024).
42. Wang, X. et al. Regulating phase homogeneity by self-assembled molecules for enhanced efficiency and stability of inverted perovskite solar cells. *Nat. Photon.* **18**, 1269–1275 (2024).
43. Siekmann, J. et al. Characterizing the influence of charge extraction layers on the performance of triple-cation perovskite solar cells. *Adv. Energy Mater.* **13**, 2300448 (2023).

# Methods

### Materials

Caesium iodide (CsI, 99.999%), *N*,*N*-dimethylformamide (DMF, anhydrous), dimethyl sulfoxide (DMSO, anhydrous), methyl acetate (MeAc, anhydrous) and 2-propanol (IPA, anhydrous) were purchased from Sigma-Aldrich. Formamidinium iodide (FAI) was purchased from Greatcell Solar Materials. Lead iodide ($PbI_2$, 99.99%), lead bromide ($PbBr_2$) and [4-(3,6-dimethyl-9H-carbazol-9-yl)butyl]phosphonic acid (Me-4PACz) were purchased from Tokyo Chemical Industry. Silver pellets were purchased from Alfa Aesar and $C_{60}$ and bathocuproine (BCP) were purchased from Luminescence Technology. PM6, Y6, P2EH and PDINN were purchased from Solarmer Materials Inc. The synthetic routes of acceptor P2EH-1V, P2EH-2V and Br-Ph-4PACz are shown in Supplementary Figs. 35–45, respectively, and the detailed synthesis processes are described in the Supplementary Notes 2 and 3.

### WBG perovskite single-junction device fabrication

The patterned ITO glass substrates were cleaned with deionized water, acetone and IPA in the ultrasonic bath for 15 min each. After ultraviolet ozone treatment for 15 min, the substrates were transferred to a nitrogen-filled glovebox and the Me-4PACz or Br-Ph-4PACz solution (1 mg ml$^{-1}$ in IPA) was spin-coated on the substrates at 4,000 r.p.m. for 30 s and heated at 100 °C for 10 min. The 1 M perovskite ($Cs_{0.25}FA_{0.75}Pb(Br_{0.4}I_{0.6})_3$) precursor solution was dissolved in 1 ml mixed solvent of DMF:DMSO (V/V = 4:1). Then the precursor solution was shaken overnight at 60 °C. For the spin-coating process, the substrate was spinning at 3,000 r.p.m. for 60 s with an acceleration of 3,000 r.p.m. s$^{-1}$ and 200 µl of MeAc was dropped at 15 s before the ending of spin-coating. To improve the wettability of the perovskite solution on Me-4PACz, we first dynamically spin-coated two small drops of perovskite solution at 4,000 r.p.m. Unlike Br-Ph-4PACz, Me-4PACz required a further 200 µl of precursor solution for better coverage. After dispensing, we removed the spin-coater chuck and gently shook the substrate, followed by the spin-coating process to form a uniform perovskite film. The perovskite films were then annealed at 100 °C for 15 min. 0.5 mg ml$^{-1}$ $EDAI_2$ IPA solution was spin-coated onto the perovskite films at a spin speed of 3,000 r.p.m. for 30 s and annealed at 100 °C for 5 min. Last, $C_{60}$ (20 nm)/BCP (8 nm)/Ag (100 nm) were deposited to complete the device fabrication.

### Organic single-junction device fabrication

15 nm $MoO_x$ was thermally evaporated on top of ITO glass. Then the substrates were transferred to a glovebox filled with nitrogen. The PM6:acceptor blend solutions (D:A = 1:1.2, 16 mg ml$^{-1}$ in total, from chloroform solution with 10 mg ml$^{-1}$ 1-bromo-3,5-dichlorobenzene as solid additive) with a total concentration of 16 mg ml$^{-1}$ were heated at 40 °C until completely dissolved. The photovoltaic performance for different donor and acceptor concentrations are presented in Supplementary Table 10. Then the solutions were spin-coated at 3,000 r.p.m. for 30 s and annealed at 100 °C for 5 min. Following this, 30 µl 1 mg ml$^{-1}$ PDINN methanol solution was spin-coated onto the organic active layers at a spin speed of 3,000 r.p.m. for 30 s. Finally, the film was transferred to the thermal evaporator system to deposit 100 nm Ag as the top electrode.

### Perovskite–organic tandem device fabrication

After completing the deposition of the $C_{60}$ layer, $SnO_x$ (20 nm) was deposited by an atomic-layer deposition system. Then the substrates were transferred to the sputter system, in which 5 nm ITO was sputtered. After that, 15 nm $MoO_x$ was thermally evaporated on top of ITO and the film was brought back to the nitrogen-filled glovebox, in which organic ink was spin-coated at 3,000 r.p.m. for 30 s and annealed at 100 °C for 5 min. Next, PDINN was deposited by spin-coating its 1 mg ml$^{-1}$ solution in methanol at 3,000 r.p.m. for 30 s. Finally, the film was transferred to the thermal evaporator system to deposit 100 nm Ag as the top electrode to complete the tandem device fabrication process.

### Device characterizations

Completed devices were masked with metal aperture masks (0.050 cm$^2$ and 1.019 cm$^2$) for *J*–*V* measurement by a Keithley 2400 source meter under simulated 1-sun AM 1.5 G illumination (100 mW cm$^{-2}$) with an ABET Technologies Sun 2000 solar simulator in a nitrogen-filled glovebox. The *J*–*V* measurements were performed in a $N_2$-filled glovebox. MPP stability tests of the devices were conducted by MPP Tracking-4B source measure unit system (Shenzhen Lancheng Technology Co., Ltd.) under a 100 mW cm$^{-2}$ white LED in ambient atmosphere at a temperature of 25 °C and about 85% relative humidity with encapsulation. EQE measurements were conducted using a Bentham PVE300-IVT system and the bias illumination obtained by 500-nm short-wave-pass filters and 800-nm long-wave-pass filters were used for the measurements of the bottom subcells and front subcells, respectively. The intensity of the LED laser used was calibrated with built-in silicon and germanium diodes before measurements. For the high-resolution EQE tests, the light was chopped at 137 Hz and coupled into a Bentham monochromator. The monochromatic light spot was focused onto the active area of the perovskite solar cell and its current under short-circuit conditions was fed to a current preamplifier (Stanford SR570) before it was analysed with a lock-in amplifier (Stanford SR830 DSP). The time constant of the lock-in amplifier was chosen to be 1 s and the preamplifier's amplification was increased to resolve low photocurrents. The EQE was determined by dividing the photocurrent of the cell by the flux of incoming photons, which was measured using a calibrated Si photodiode. All EQE measurements were conducted in an ambient atmosphere with a temperature of 25 °C and about 60% relative humidity with encapsulation. Cross-sectional scanning electron microscopy images of devices were taken with the Regulus SU8200 system (Hitachi) at 5 kV accelerating voltage under SE mode. The electroluminescence emission spectra were acquired by a combination of NOVA and NIR1700 spectrometers (Fuxiang Inc.). The voltage bias was applied to devices with a Keithley 2400 external voltage/current source meter. Sensitive EQE was recorded by Fourier-transform photocurrent spectroscopy (PECT-600, Enli Technology Co., Ltd.). $EQE_{EL}$ measurements were performed by applying external voltage/current sources through the devices (ELCT-3010, Enlitech).

### Material characterizations

Steady-state PL and PL evolution measurements were taken using a LP20-32 radiative efficiency meter (Quantum Yield Berlin). The built-in 532-nm laser was switched on 15 min in advance to allow warm-up and stabilization. All of the PL spectra were recorded under 1-sun 532-nm laser illumination. GIWAXS was conducted at beamline TPS25A1 at the National Synchrotron Radiation Research Center (NSRRC, Hsinchu, Taiwan). A monochromatic X-ray beam with an energy of 15 keV and a beam size of 5 × 5 µm$^2$ was used. The samples were probed at an incident angle of 0.16°. The sample-to-detector distance was 101.1 mm, which was calibrated by a $CeO_2$ sample. The images were captured in two dimensions using a single-photon counting detector, the Eiger X 1M, with a pixel size of 75 µm, and the obtained images were analysed by the INSIGHT software package. All samples were measured under a nitrogen-filled closed chamber.

AFM measurements were performed with non-contact mode. Sideband KPFM measurements were performed under EFM (non-contact) mode. The work function was calibrated before every sample with a standard gold reference sample. Also, the signals were optimized in advance by applying bias voltage onto the samples in advance of the measurements.

### Femtosecond transient absorption spectra

Femtosecond transient absorption spectroscopy measurements were performed on an Ultrafast Helios pump–probe system in collaboration with a regenerative amplified laser system from Coherent. An 800-nm pulse with a repetition rate of 1 kHz, a length of 100 fs and an energy of 7 mJ pulse$^{-1}$ was generated by a Ti:sapphire amplifier (Astrella, Coherent). Then the 800-nm pulse was separated into two parts by a beam splitter. One part was used as the pump beam to excite the samples and the other part was focused onto a sapphire plate and a YAG plate to generate white-light supercontinuum as the probe beams with spectra covering 420–800 nm and 750–1,600 nm, respectively. The time delay between pump and probe was controlled by a motorized optical delay line with a maximum delay time of 8 ns. The pump pulse is chopped by a mechanical chopper with a frequency of 500 Hz and then focused onto the mounted sample with probe beams. The probe beam was collimated and focused into a fibre-coupled multichannel spectrometer with a charge-coupled device sensor. The energy of the pump pulse was measured and calibrated by a power meter (PM400, Thorlabs). The films were spin-coated onto 1-mm-thick quartz plates and encapsulated by epoxy resin in a nitrogen-filled glovebox to resist water and oxygen in air.

## Data availability

The data that support the findings of this study are available from the corresponding author on request.

**Acknowledgements** Y.H. acknowledges the support from the Agency for Science, Technology and Research (A*STAR) under its MTC Individual Research Grants (232K2087). The authors of this paper are affiliated with the Solar Energy Research Institute of Singapore (SERIS), a research institute at the National University of Singapore (NUS). SERIS is supported by the NUS, the National Research Foundation Singapore (NRF), the Energy Market Authority of Singapore (EMA) and the Singapore Economic Development Board (EDB). P.M.-B. acknowledges support by the Deutsche Forschungsgemeinschaft (DFG, German Research Foundation) under Germany's Excellence Strategy – EXC 2089/1 – 390776260 (e-conversion) and through TUM.solar in the context of the Bavarian Collaborative Research Project Solar Technologies Go Hybrid (SolTech). The simulation works for this article were entirely performed on resources of the National Supercomputing Centre (NSCC) Singapore (https://www.nscc.sg). Part of this work was carried out at PETRA III and we would like to thank J. Zhang, A. Buyan-Arivjikh, A. Chumakov and M. Schwartzkopf for their assistance with the measurements at the P03 beamline.

**Author contributions** Z.J. and Y.H. conceived the idea and designed the experiments. Y.H. supervised the project. Z.J. synthesized and characterized the acceptors. Z.J. and X.G. fabricated and characterized the tandem cells. X.G. conducted device characterizations of the WBG perovskite solar cells. X.Y. synthesized the SAM material. M.S. and X.D. measured and analysed the energy loss of the organic solar cells. J.Q. and X.H. measured and analysed transient absorption spectroscopy. R.G., X. Jiang, S.V.R., P.M.-B. and C.-H.K. performed GIWAXS measurements and analysed the data. X.W. conducted contact-angle measurements. Y.W. completed the cross-sectional scanning electron microscopy imaging. Z.D. completed the KPFM and AFM imaging. Z.S. contributed to density functional theory simulations. Q.Z., Z.W., S.L. and L.K.L. participated in the device fabrication and characterizations for the single-junction solar cells. J.H. completed the transmission electron microscopy imaging. X. Jia assisted with $V_{\mathrm{OC}}$ loss analysis. J.C. and H.L. conducted ultraviolet photoelectron spectroscopy measurements. N.L. conducted transient photovoltage measurements. Z.J. and Y.H. analysed the results and wrote the manuscript.

**Competing interests** The authors declare no competing interests.

**Additional information**

**Supplementary information** The online version contains supplementary material available at https://doi.org/10.1038/s41586-025-09181-x.

**Correspondence and requests for materials** should be addressed to Yi Hou.

**Peer review information** *Nature* thanks Ashish Kulkarni, Chang Eun Song and the other, anonymous, reviewer(s) for their contribution to the peer review of this work.